On the analysis of notched concrete beams: From measurement with Digital Image Correlation to identification with Boundary Element Method of a cohesive model

Manuel D.C. Ferreira, Wilson Venturini, François Hild

On the analysis of notched concrete beams: From measurement with Digital Image Correlation to identification with Boundary Element Method of a cohesive model

M.D.C. Ferreira,[1] W.S. Venturini[1] and F. Hild[2-*]

[1]Departamento de Engenharia de Estruturas, Escola de Engenharia de São Carlos

Universidade de São Paulo

Av. Trabalhador São-Carlense, 400 - CEP 13566-590 - São Carlos, SP – Brasil

E-mail: {mdenis,venturin}@sc.usp.br

[2]LMT-Cachan, ENS Cachan / CNRS / UPMC / PRES UniverSud Paris

61 avenue du Président Wilson, F-94235 Cachan Cedex, France

E-mail: hild@lmt.ens-cachan.fr

[*]Corresponding author. Email: hild@lmt.ens-cachan.fr, Fax: +33 1 47 40 22 40.

On the analysis of notched concrete beams: From measurement with Digital Image Correlation to identification with Boundary Element Method of a cohesive model

by

M.D.C. Ferreira, W.S. Venturini and F. Hild

Abstract

A way of coupling digital image correlation (to measure displacement fields) and boundary element method (to compute displacements and tractions along a crack surface) is presented herein. It allows for the identification of Young's modulus and fracture parameters associated with a cohesive model. This procedure is illustrated to analyze the latter for an ordinary concrete in a three-point bend test on a notched beam. In view of measurement uncertainties, the results are deemed trustworthy thanks to the fact that numerous measurement points are accessible and used as entries to the identification procedure.

Keywords: *boundary elements, cohesive crack, digital image correlation, inverse analysis, parameter identification.*

Nomenclature

Γ	external boundary of domain Ω
Γ_1 , Γ_1^e	boundary, external boundary of domain Ω_1
Γ^i	interface between domains Ω_1 and Ω_2
Δu, Δu_c	crack opening displacement, critical value
μ	Lamé's coefficient
ν	Poisson's ratio
Ω	considered domain
Ω_1 , Ω_2	two sub-domains separated by an interface
Ω_j , Ω_k	sub-domain Ω_1 or Ω_2, sub-domain Ω_2 or Ω_1
σ_u	displacement uncertainty
A	parameter
$[A_i^u]$	global matrix
$\{b_i^{p-m}\}$	global vector
C_{ik}	free term of the boundary integral equations
E	Young's modulus
f_t , f_t^c	opening traction on the interface, critical traction
F	function defining the cohesive law

G_c toughness

$[G_i^u]$, $[G_i'^u]$ matrices obtained by carrying out the integrals over boundary and interface elements for unknown displacements and tractions on the interface

$[G_k^p]$, $[G_k^u]$ matrices obtained by carrying out the integrals over boundary and interface elements for prescribed, unknown tractions

$[G_k'^p]$, $[G_k'^u]$ matrices obtained by carrying out the integrals over boundary and interface elements for prescribed, unknown tractions when considering inner points

$[G_{kk}]$, $[G_{kj}]$ matrices obtained by carrying out integrals over boundary and interface elements

$[G'_{kk}]$, $[G'_{kj}]$ matrices obtained by carrying out the integrals over boundary and interface elements when considering internal points

$[H_i^u]$, $[H_i'^u]$ matrices obtained by carrying out the integrals over boundary and interface elements for unknown displacements and tractions on the interface

$[H_k^p]$, $[H_k^u]$ matrices obtained by carrying out the integrals over boundary and interface elements for prescribed, unknown displacements

$[H_k'^u]$, $[H_k'^p]$ matrices obtained by carrying out the integrals over boundary and interface elements for prescribed, unknown tractions when considering inner points

$[H_{kk}]$, $[H_{kj}]$ matrices obtained by carrying out the integrals over boundary and interface elements

$[H'_{kk}]$, $[H'_{kj}]$ matrices obtained by carrying out the integrals over boundary and interface elements when considering internal points

K_c	critical stress intensity factor
ℓ	element size in the DIC analysis
M	point on the boundary and in the domain
p_{ik}^{*}	fundamental Kelvin's solutions for the tractions induced by a unit point load applied to a collocation point S on the external boundary
p_k	boundary traction
$\{ p_k \}, \{ p_{kj} \}$	vectors containing the boundary and interface tractions
$\{p_k^p\}, \{p_k^u\}$	prescribed and unknown tractions on the boundary
$\{p_i^u\}$	unknown tractions on the interface
S	collocation point
$\{ u_i \}$	vectors containing the nodal displacements of internal points
u_{ik}^{*}	fundamental Kelvin's solutions for the displacements induced by a unit point load applied to a collocation point S on the external boundary
u_i^u	unknown displacements on the interface
u_k	boundary displacement
$\{ u_k \}, \{ u_{kj} \}$	vectors containing the boundary and interface nodal displacements
$\{u_k^p\}, \{u_k^u\}$	prescribed and unknown nodal displacements on the boundary
$\{ u_k^m \}$	measured displacements for internal points in domain
$\{v_i^{p-m}\}$	contribution of the known data

$\{v_k^{p-m}\}$	contribution of the known data
w	width of the sample
$\{w_i^{p-m}\}$	contribution of the known data
$\{w_k^{p-m}\}$	contribution of the known data
$\{x_i^u\}$	vector gathering all unknowns (displacements and tractions)

1. Introduction

One way of numerically analyzing cracked samples or structures is to resort to cohesive models. Since the pioneering works of Dugdale [1], Barenblatt [2] and Hillerborg et al. [3, 4], these models have become very popular [5, 6 , 7, 8 , 9], in particular when dealing with concrete materials. One of the open questions concerns the identification of cohesive laws in a robust way since, in many instances, only strain and load data are available [10]. In addition to global data, pictures shot at different scales are also used in a qualitative way [11, 12, 13, 14] or a more quantitative way by measuring deflections [15, 16] and deformed shapes [17]. Full-field measurements provide very useful data to identify interface behaviors [18, 19]. In the present paper, it is proposed to use displacement measurements to calibrate the cohesive law. The calibration is performed by resorting to an inverse analysis using the kinematic data as inputs.

Inverse analyses are nowadays a very important tool in many engineering fields. In solid mechanics, the technique is applied mainly to identify, for instance, material properties, boundary conditions, material degradation, crack formation, which are parameters needed to check the structural safety. Identification or inversion procedures are mainly applied by using finite-element-based procedures [20] coupled with full-field measurements [21]. Full-field measurements [22] are generally performed by analyzing the motion and deformation of external surfaces (e.g., by resorting to digital image correlation (DIC) [23]). This specific feature motivates the work presented herein that aims at combining displacement fields measured by DIC and simulations with the boundary element method (BEM) to extract the parameters of a cohesive law describing cracking in concrete.

As for many applications in engineering, the boundary element method (BEM) is a numerical technique very appropriate to perform inverse analyses. The method is recommended when a fine analysis is required only over a small region of the body. The

method is also very accurate for problems in which high gradients may occur. These situations are often found in inverse problems (e.g., when dealing with damage and cracks). There are several works developed so far using boundary element methods for parameter identification in structural analyses [24, 25, 26, 27, 28] in the context of deterministic approaches. There are also several other developed works based on stochastic techniques [29, 30, 31]. In all these works, BEM-based procedures are proposed to deal with material property identification in solid mechanics. However, experimental data were only used in the work of Tin-Loi and Que [30] to show the efficiency of the developed method.

In this work a simple technique based on the BEM singular formulation is used to identify cohesive crack parameters of a concrete beam that is tested up to complete failure. BEM crack singular formulations [32] may also be considered. Three-point bend test is performed on a notched specimen (Section 3). To perform the inverse analysis, only singular equations (i.e., based upon a kinematic formulation [33, 34]) are used in the region monitored during the experiment by a camera (Section 2). The latter provides pictures that are used to measure displacement fields by DIC that are entries to the inverse analysis. The BEM algebraic system of equations enables for the computation of crack openings and tractions for which least squares are used to extract Young's modulus and the parameters of a linear cohesive law (Section 4).

2. Boundary element approach for inverse analyses

For an elastic multi-region body that, for the sake of simplicity, is assumed to be formed of two regions Ω_1 and Ω_2 (Figure 1) separated by an interface (e.g., a crack) the following integral boundary equation expresses equilibrium of each region

$$C_{ik}(S)u_k(S) + \int_\Gamma p^*_{ik}(S,M)u_k(M)d\Gamma = \int_\Gamma u^*_{ik}(S,M)p_k(M)d\Gamma \qquad (1)$$

where p_{ik}^{*} and u_{ik}^{*} are fundamental Kelvin's solutions for the tractions and displacements induced by a unit point load applied to a collocation point *S* on the boundary, inside or outside the domain, *M* points on the boundary and in the domain, respectively, and C_{ik} is the well-known free term of the boundary integral equations [35]. Boundary Γ_1 of domain Ω_1 is given by the union of the external contour Γ_1^e and the interface Γ^i with domain Ω_2, i.e., $\Gamma_1 = \Gamma_1^e \cup \Gamma^i$. The cohesive law will be anlyzed along the interface Γ^i.

For direct analyses, Equation (1) is transformed into an algebraic system of equations that is solved directly after taking into account the boundary conditions. To obtain the algebraic representations the boundary and the interface of sub-domains Ω_1 and Ω_2 are discretized by using elements and approximate displacements and tractions along them. For a given sub-region Ω_k the following algebraic representations are obtained

$$[H_{kk} \quad H_{kj}]\begin{Bmatrix} u_k \\ u_{kj} \end{Bmatrix} = [G_{kk} \quad G_{kj}]\begin{Bmatrix} p_k \\ p_{kj} \end{Bmatrix} \tag{2}$$

where Ω_j is the other sub-domain, matrices $[H_{kk}]$, $[G_{kk}]$, $[H_{kj}]$ and $[G_{kj}]$ are obtained by carrying out the integrals over boundary and interface elements, respectively, vectors $\{u_k\}$, $\{u_{kj}\}$ contain the boundary and interface nodal displacements, while $\{p_k\}$ and $\{p_{kj}\}$ contain the boundary and interface tractions.

Similarly, the algebraic relationships written conveniently only for internal points are given by

$$\{u_i\} = -[H'_{kk} \quad H'_{kj}]\begin{Bmatrix} u_k \\ u_{kj} \end{Bmatrix} + [G'_{kk} \quad G'_{kj}]\begin{Bmatrix} p_k \\ p_{kj} \end{Bmatrix} \tag{3}$$

Equations (2) and (3), the equilibrium and displacement compatibility at all interface nodes are needed to solve the problem and to obtain the displacement field inside the solid where required.

In the sequel, the inverse procedure based on a BEM formulation is applied to identify cohesive law parameters. Thus, the sub-region equations given above for the two sub-regions are further simplified. Both sub-regions are assumed to be made of the same (elastic) material described by Lamé's coefficient μ and Poisson's ratio ν. They can be easily found either by using appropriate tests with the uncracked material or by applying, say, the least squares method to load vs. displacement curves during the initial loading process where an elastic phase is assumed. This point is solved differently herein by considering an internal point. Therefore, to derive the algebraic system of equations for the crack cohesive parameter identification, the elastic parameters of both sub-regions are assumed to be known.

For inverse problems, Equations (2) and (3) have to be properly modified. Let us consider that the boundary value vector for the sub-region Ω_k contains the following prescribed values $\{u_k^p\}$ and $\{p_k^p\}$. The remaining boundary values and the interface displacement and traction values are *unknown* and stored in $\{u_k^u\}$ and $\{p_k^u\}$, respectively. All combinations between prescribed and unknown values at boundary nodes are allowed. Thus, a single node may have all boundary values either completely known, or totally unknown, or any other possible combination thereof. Subdividing the matrices in Equations (2) and (3) yields

$$[H_k^u \quad H_k^p]\begin{Bmatrix} u_k^u \\ u_k^p \end{Bmatrix} = [G_k^u \quad G_k^p]\begin{Bmatrix} p_k^u \\ p_k^p \end{Bmatrix} \tag{4}$$

$$\{u_k^m\} = -[H_k'^u \quad H_k'^p]\begin{Bmatrix} u_k^u \\ u_k^p \end{Bmatrix} + [G_k'^u \quad G_k'^p]\begin{Bmatrix} p_k^u \\ p_k^p \end{Bmatrix} \tag{5}$$

where $\{u_k^m\}$ are the displacements measured during the experiment at a certain number of internal points. It is important to stress that there is no relationship between the numbers of columns defined by the prescribed (p) and unknown (u) boundary values. The size of the boundary displacement unknown vector $\{u_k^u\}$ is independent of that of the prescribed traction vector $\{p_k^u\}$. The minimum number of known boundary values is zero. Therefore, Equation (5) is written only for points where the displacements are known. Depending on the process used to measure these displacements, the number of relationships in Equations (4) and (5) is very large, leading to a large number of redundant equations that is very important for the minimization process to be applied.

Equations (4) and (5) are joined together to define a system in which the unknowns are moved to the left hand side

$$\begin{bmatrix} H_k^u & -G_k^u \\ H_k'^u & -G_k'^u \end{bmatrix} \begin{Bmatrix} u_k^u \\ p_k^u \end{Bmatrix} = \begin{Bmatrix} v_k^{p-m} \\ w_k^{p-m} \end{Bmatrix} \tag{6}$$

where $\{v_k^{p-m}\}$ and $\{w_k^{p-m}\}$ contain the contribution of the known values including the measured displacements at internal points.

A similar system of algebraic equations is written for sub-region Ω_j. They are joined together after assuming the displacement compatibility and equilibrium conditions along the interface (i.e., given by the chosen cohesive law). The same format as Equation (6) is obtained but the displacement and traction vectors are modified accordingly to extract the boundary displacements and tractions of the two regions in addition to the interface values $\{u_i^u\}$ and $\{p_i^u\}$. The contribution of the prescribed boundary values and the measured displacements are now stored in $\{v_i^{p-m}\}$ and $\{w_i^{p-m}\}$. Thus, the final system reads

$$\begin{bmatrix} H_i^u & -G_i^u \\ H_i'^u & -G_i'^u \end{bmatrix} \begin{Bmatrix} u_i^u \\ p_i^u \end{Bmatrix} = \begin{Bmatrix} v_i^{p-m} \\ w_i^{p-m} \end{Bmatrix} \tag{7}$$

or equivalently

$$[A_i^u]\{x_i^u\} = \{b_i^{p-m}\} \tag{8}$$

Equation (8) is a redundant system with a very large number of algebraic relationships usually written for the region of interest where the displacement field is measured. In that case all boundary values are unknown and the redundancy is guaranteed by the large number of internal points where the displacements are known. It is solved using any identification technique to obtain the unknown vector $\{x_i^u\}$. The least squares technique [36] is the simplest tool to determine the solution to Equations (8)

$$[A_i^u]^t[A_i^u]\{x_i^u\} = [A_i^u]^t\{b_i^{p-m}\} \tag{9}$$

Alternative approaches are given by Tikhonov's regularization technique [37] or the singular value decomposition (SVD) approach [38]. They are not reported herein, even though they were already used to analyze artificial test cases [39]. Kalman filters can also be used [40].

After obtaining the profiles of tractions $\{p_i^u\}$ and crack opening displacements (based upon the interfacial displacements $\{u_i^u\}$), the parameters of the cohesive model are to be determined. As for any non-linear model, the yield surface *F* of the cohesive model reads

$$F(f_t, \Delta u) = 0 \tag{10}$$

where f_t is tensile (opening) traction in the direction perpendicular to the crack surface, and Δu the corresponding crack opening displacement.

To identify the cohesive parameters, a "regularized" system of Equations (9) for which interpenetration is avoided, *i.e.* the crack opening displacement is set to zero if a negative

value were obtained in the previous iteration. The system given in Equation (9) is then reordered accordingly. After obtaining the displacement jump and tractions along the crack line, a regression is used to identify the limit surface using a chosen number of parameters. Assuming a linear limit surface to describe the cohesive model

$$F(f_t, \Delta u) = f_t - f_t^c (1 - \Delta u / \Delta u_c) = 0 \tag{11}$$

the unknown parameters are f_t^c and Δu_c. They correspond to the maximum values of the traction and crack opening displacement allowing for load transfer, respectively.

3. Experimental analysis

A three-point flexural test was performed on a regular concrete specimen. The sample size is ca. $150 \times 150 \times 500$ mm^3, the notch depth is 25 mm and its width 3 mm. The outer span is of the order of 450 mm (Figure 2). The experiment is controlled by using the signal delivered by a clip gauge installed on the lower face of the sample (i.e., the notch opening displacement is regulated). Furthermore, DIC is used to evaluate the displacement fields on one lateral surface of the sample. DIC is an optical technique to measure displacement fields of a surface [23] by registering pictures of the surface for different states, one before loading being the reference state, and the other one when load is applied. In the present case, only one camera is used since the out-of-plane displacements are vanishingly small. By implementing the brightness conservation equation, different displacement kinematics are measurable in a global setting [41]. In the present case, a so-called Q4-DIC algorithm is used [42]. It consists in decomposing the displacement field into components associated with shape functions identical to those used, for instance, in finite element approaches. The location of the region of interest (ROI) is depicted in Figure 2. A semi-professional camera is used to acquire pictures (Canon EOS 30D, 12-bit RGB CMOS sensor delivering $3{,}504 \times 2{,}336$-pixel images).

The sample surface was prepared by using black and white paint. The texture is obtained by using a mask with an array of holes (Figure 2).

3.1. Displacement resolution

For measurement and identification purposes, it is important to assess the accuracy of the experimental results obtained by using a correlation algorithm. The displacement resolution is estimated by considering consecutive pictures when no load is applied, and running correlation analyses. The displacement resolution is estimated when the correlation parameters are modified. In particular, the effect of the element size ℓ expressed in pixels on the displacement resolution is investigated. The quality of the estimate is therefore characterized by the standard displacement resolution, σ_u, which is defined as the mean of all the standard displacement resolutions. Figure 3 shows the standard displacement resolution σ_u as a function of the element size ℓ. The larger the element size, the smaller the resolution. For the analyzed element sizes, a power law with an exponent α of the order 1 is found

$$\sigma_u = \frac{A^{\alpha+1}}{\ell^{\alpha}} \tag{12}$$

with $A = 0.7$ pixel, thereby indicating that the displacement resolution and the corresponding spatial resolution (or element size ℓ) are the result of a compromise. In the following, 16-pixel elements are considered.

A first analysis using displacement measurements consists in comparing the output of the clip gauge to an average displacement jump computed as the horizontal displacement difference between two zones chosen around the notch (Figure 4). The element size is equal to 16 pixels on quarter resolution pictures to perform the analysis on a conventional PC. The analysis is performed for a sequence of 60 pictures. Figure 5a shows the load / notch opening

measured by the clip gauge. The points when the pictures were shot are also depicted. With the used concrete sample, a gradual softening occurs.

Figure 5b shows a comparison of the clip gauge data and those obtained by post-processing the displacement field. Even though the measurement locations are different (Figure 2), a quasi linear trend is observed when the two outputs are compared. In terms of identification residuals, a root mean square value of 2.4 μm (or 0.04 pixel) is found. This result shows that the DIC technique yields results consistent with those obtained by the clip gauge, and constitutes a first validation of DIC to analyze the present test. From the previous resolution analysis, the standard displacement resolution is of the order of 0.03 pixel (or 1.5 μm). The value of the displacement jump remains in the subpixel range (i.e., less than 54 μm) during a significant part of the load history (Figure 5b), yet significantly larger than the measurement resolution. By visual inspection of the picture it is impossible to detect the presence of the crack. Consequently, the present analysis is only made possible by using DIC.

The next step is to analyze the displacement field over the whole ROI (more than 8,900 nodes are used when an element size of 16 pixels is chosen). Figure 6 shows five displacement maps in the softening part of the load vs. notch opening curve. As the notch opening increases the crack propagates. From the displacement contours, it is possible to locate the crack surface.

Last, the crack surface and the corresponding displacement jump are sought. To determine the crack surface, the contour of 0-horizontal displacement is determined (Figure 7b) when the rigid body motion was subtracted from the measured displacement field (Figure 7a). This procedure is applied to a picture after failure for which the horizontal displacement map is shown in Figure 8. To check this evaluation, the actual surface in the deformed picture is compared with the profile obtained when the surface of Figure 7b is translated with the

measured displacement field evaluated along the latter. A good agreement is obtained (Figure 8) and gives confidence in the following results. The crack surface is depicted in Figure 6 and the 0-contours. These two quantities allow one to compare the current crack surface and that determined at the very end of the experiment. A good match is observed except for a vertical interval ranging from 1300 to 1500 pixels, and from 200 to 400 pixels. A closer look at Figure 8 in this area shows that there is not a unique crack but two branches that are very close to each other.

The crack opening displacements are obtained when considering the displacement jump of two points located symmetrically from the crack surface. A distance of two element sizes (i.e., 32 pixels) is chosen (see dashed lines of Figure 7b). Figure 9 shows the change of the crack opening displacement for the five pictures analyzed in Figure 6. This plot shows the difficulty of the identification because data are noisy (i.e., the displacement levels are very small), and therefore calls for robust procedures and a large amount of data (here provided by DIC results).

4. Identification

For the experiment described in the previous section an inverse analysis is carried out to identify the parameters of the cohesive law. First, the elastic properties of the concrete beam are identified. Then, using the model presented in Section 2 the sought parameters are identified.

4.1. Elastic properties

Although inserting the elastic modulus as an unknown in Equation (7) is very simple, the BEM-based inverse analysis is not used to find the elastic parameters. Instead, the measured displacement at an internal point is used to estimate the elastic modulus. The fine boundary element discretization adopted to construct the applied force vs. displacement curve of the

beam is shown in Figure 10. The measured displacements at the chosen internal point are given in Figure 11, where a clear linear relationship is observed after the second load increment. Thus, to evaluate Young's modulus E, the initial part of the curve is discarded and the non-linear part where the crack propagation effects are observed. Comparing this measured slope with the one obtained numerically, an average Young's modulus for this concrete beam is found to be $E = 18$ GPa. This value is significantly smaller than the Young's modulus measured directly by carrying out standard compression tests on cylindrical specimens cast with this concrete, $E = 30$ GPa. This may be due to the coarseness of the microstructure of the material studied herein. Poisson's ratio cannot be measured by this procedure because the displacement level is too small in comparison to the displacement resolution. A value of $\nu = 0.2$, obtained using cylindrical specimens is considered in the present analysis. It is important to stress that although the elastic parameters were identified in this part, their influence on the final analysis to identify the cohesive crack parameters is very small.

4.2. Cohesive model

Having identified the elastic parameters, the inverse analysis is now carried out for the sub-domain of interest indicated in Figure 2. Only a small region around the crack line is considered where the pictures shot during the experiment brought important information regarding displacement fields. This region of interest is discretized by using 81 boundary elements, while the crack line was also approximated by using 104 elements, as shown in Figure 12. The crack surface has been approximated by several straight paths. Therefore, small boundary fluctuations are "ironed out" and only the main corners are conserved to carry out this analysis.

The analyzed region contains the crack line shown in Figure 12 and is analyzed by using the proposed BEM-based inverse procedure. The displacement values read at ca. 1200

internal points and boundary points are prescribed to obtain the crack opening displacements and the corresponding traction distribution along the crack line as shown in Figures 13 and 14. After plotting the computed crack opening displacements vs. tractions along the crack surface, several points corresponding exactly at assumed kinks were completely out of the expected distribution showing the local effects that are presumably due to aggregate interlocking. Consequently, it was decided to use only the points related to the smooth parts of the crack surface also including some corners that did not show strong effects.

Figures 15 and 16 show the crack opening displacements as a function of tractions along the two most important parts of the crack surface. These parts are defined between nodes 09 and 23 (Figure 15) and nodes 25 and 35 (Figure 16). It is worth noting that when analyzing the data with the error bars (a displacement uncertainty equal to $3\sigma_u = 4.5$ µm is considered), all the computed displacement data fall within that zone. When considering these two separate groups of points, the corresponding regressions lead to different cohesive parameters. Next, the results obtained for all the points are put together. Figure 17 shows the final results and the approximated curve obtained by regression. The gray zone accounts for a measurement uncertainty of $\pm 3\sigma_u$. There is only one point that lies outside this confidence domain. Consequently, it is assumed that the chosen cohesive law describes reasonably the behavior of cracks in that type of concrete. From this approximation, the following cohesive law parameters are found $f_t^c = 860$ kN / mm and $\Delta u_c = 0.023$ mm. With these values, the toughness becomes $G_c = f_t^c \, \Delta u_c / 2 \; w = 66$ J/m^2, and the corresponding critical stress intensity factor $K_c \approx \sqrt{EG_c} = 1.1$ MPa$\sqrt{\text{m}}$. This level lies in the range of values for ordinary concrete ($0.2 \le K_c \le 1.4$ MPa$\sqrt{\text{m}}$). The fact that the identified value is close to the upper bound indicates that the aggregates played a role in crack propagation that is not straight (Figure 8).

5. Summary and perspectives

In this paper it was proposed to couple DIC and BEM to identify mechanical properties. An experimental test on ordinary concrete was performed. In the present case, displacement fields measured with Q4-DIC were used. It is worth noting that this test is very difficult to analyze since the displacement levels are very small. However it was shown that even with noisy input data, the fact that they were numerous made possible the identification of Young's modulus and the two parameters of a linear cohesive law.

By using the displacement resolution evaluated directly during the experiment, it was shown that the identification results are obtained with a good confidence interval. The fact that parameters identified in the present case lead to a fracture toughness that lies within the bounds associated with ordinary concrete is an additional proof. These two features show that coupling DIC and BEM is a viable route to identify elastic and fracture properties of concrete. This type of procedure may be applied to other quasi-brittle materials such as composites or other geomaterials.

Last, it is worth remembering that the numerical analyses performed herein were two-dimensional. In view of the crack surface, it is likely that 3D analyses are more than desirable for more accurate estimates of the parameters of the cohesive law. However, there is then a need for the identification of the crack surface in addition to the information given by pictures of only one surface of the sample. Two routes can be followed. First, by using two cameras the shape of the crack surface would be known on both sides of the sample. The way they connect would either be assumed or left as an additional unknown to be identified. Second, digital volume correlation [43] could be used as the sample would be imaged in a tomograph. This technique was shown to be able to extract, for instance, the crack surface and profiles of stress intensity factors [44], and to compare them with numerical simulations with, say, X-FEM [44, 45]. Analyses with BEM could also be considered.

Acknowledgments

This work was performed with the support of a FAPESP/CNRS project.

References

[1] Dugdale, D.S., Yielding of Steel Sheets Containing Slits, *J. Mech. Phys. Solids*, **8**, pp. 100-104, 1960

[2] Barenblatt, G.I., The Mathematical Theory of Equilibrium of Crack in Brittle Fracture, *Adv. Appl. Mech.*, **7**, pp. 55-129, 1962

[3] Hillerborg, A., Modeer, M., Petersson, P.E., Analysis of crack formation and crack growth in concrete by means of fracture mechanics and finite elements, *Cement Conc. Res.*, **6**, pp. 773-782, 1976

[4] Petersson, P.E., Crack growth and development of fracture zone in plain concrete and similar materials, Lund University (Sweden), Report TVBM-1006, 1981

[5] Xu, X.P., Needleman, A., Void nucleation by inclusions debonding in a crystal matrix, *Modelling Simul. Mater. Sci. Eng.*, **1**, pp. 111-132, 1993

[6] Bažant, Z.P., Concrete fracture models: Testing and practice, *Eng. Fract. Mech.*, **69**, pp. 165-205, 2002

[7] Elices, M., Guinea, G.V., Gomez, F.J., Planas, J., The cohesive zone model: Advantage, limitations and challenges, *Eng. Fract. Mech.*, **69**, pp. 137-163, 2002

[8] Planas, J., Elices, M., Guinea, G.V., Gomez, F.J., Cendon, D.A., I., A., Generalizations and specializations of cohesive crack models, *Eng. Fract. Mech.*, **70**, pp. 1759-1776, 2003

[9] de Borst, R., Remmers, J., Needleman, A., Mesh-independent numerical representations of cohesive-zone models, *Eng. Fract. Mech.*, **173**(2), pp. 160-177, 2006

[10] Derewonko, A., Godzimirski, J., Kosiuczenko, K., Niezgoda, T., Kiczko, A., Strength assessment of adhesive-bonded joints, *Comput. Mat. Sci.*, **43**(1), pp. 157-164, 2008

[11] Pardoen, T., Ferracin, T., Landis, C.M., Delannay, F., Constraint effects in adhesive joint fracture, *J. Mech. Phys. Solids*, **53**, pp. 1951–1983, 2005

[12] Leffler, K., Alfredsson, K.S., Stigh, U., Shear behaviour of adhesive layers, *Int. J. Solids Struct.*, **44**, pp. 530-545, 2007

[13] Salomonsson, K., Andersson, T., Modeling and parameter calibration of an adhesive layer at the meso level, *Mech. Mat.*, **40**(1-2), pp. 48-65, 2008

[14] Sørensen, B.F., Gamstedt, E.K., Østergaard, R.C., Goutianos, S., Micromechanical model of cross-over fibre bridging – Prediction of mixed mode bridging laws, *Mech. Mat.*, **40**, pp. 220-234, 2008

[15] Yang, Q.D., Thouless, M.D., Ward, S.M., Elastic-plastic mode-II fracture of adhesive joints, *Int. J. Solids Struct.*, **38**, pp. 3251-3262, 2001

[16] Su, C., Wei, Y.J., Anand, L., An elastic–plastic interface constitutive model: Application to adhesive joints, *Int. J. Plasticity*, **20**, pp. 2063–2081, 2004

[17] Sargent, J.P., Durability studies for aerospace applications using peel and wedge tests, *Int. J. Adhesion Adhesives*, **25**, pp. 247–256, 2005

[18] Abanto-Bueno, J., Lambros, J., Experimental Determination of Cohesive Failure Properties of a Photodegradable Copolymer, *Exp. Mech.*, **45**(2), pp. 144-152, 2005

[19] Fedele, R., Raka, B., Hild, F., Roux, S., Identification of adhesive properties in GLARE assemblies by Digital Image Correlation, *J. Mech. Phys. Solids*, **57**, pp. 1003-1016, 2009

[20] Bonnet, M., Constantinescu, A., Inverse problems in elasticity, *Inverse Problems*, **21**, pp. R1-R50, 2005

[21] Avril, S., Bonnet, M., Bretelle, A.-S., Grédiac, M., Hild, F., Ienny, P., Latourte, F., Lemosse, D., Pagano, S., Pagnacco, E., Pierron, F., Overview of identification methods of mechanical parameters based on full-field measurements, *Exp. Mech.*, **48**(4), pp. 381-402, 2008

[22] Rastogi, P.K., *Photomechanics*, Springer, Berlin (Germany), 2000

[23] Sutton, M.A., Orteu, J.-J., Schreier, H., *Image correlation for shape, motion and deformation measurements: Basic Concepts, Theory and Applications*, Springer, 2009

[24] Mellings, S.C., Aliabadi, M.H., Flaw identification using the boundary element method, *Int. J. Num. Meth. Eng.*, **38**(3), pp. 399-419, 1995

[25] Alessandri, C., Mallardo, V., Crack identification in two-dimensional unilateral contact mechanics with the boundary element method, *Comput. Mech.*, **24**(2), pp. 100-109, 1999

[26] Comino, L., Gallego, R., Material constants identification in anisotropic materials using boundary element techniques., *Inverse Problems Sci. Eng.*, **13**(6), pp. 635-654, 2005

[27] Engelhardt, M., Stavroulakis, G.E., Antes, H., Crack and flaw identification in elastodynamics using Karman filrter techniques., *Comput. Mech.*, **37**(3), pp. 249-265, 2006

[28] Nemitz, N., Bonnet, M., Topological sensitivity and FMM-accelerated BEM applied to 3D acoustic inverse scattering, *Eng. An. Bound. Elem.*, **32**(11), pp. 957-970, 2008

[29] Burczynski, T., Beluch, W., The identification of cracks using boundary elements and evolutionary algorithms, *Eng. An. Bound. Elem.*, **25**, pp. 313, 2001

[30] Tin-Loi, F., Que, N.S., Identification of cohesive crack fracture parameters by evolutionary search, *Comput. Meth. Appl. Mech. Eng.*, **191**(49-50), pp. 5741-5760, 2002

[31] Engelhardt, M., Schanz, M., Stavroulakis, G.E., Antes, H., Defect identification in 3-D elastostatics using a genetic algorithm, *Optimiz. Eng.*, **7**(1), pp. 63-79, 2006

[32] Aliabadi, M.H., Boundary element formulations in fracture mechanics, *Appl. Mech. Reviews*, **50**, pp. 83-96, 1997

[33] Blandford, G.E., Ingraffea, A.R., Ligget, J.A., Two-dimensional Stress Intensify Factor computations using the Boundary Element Method, *Int. J. Num. Meth. Eng.*, **17**, pp. 387-404, 1981

[34] Liang, R.Y., Li, Y.N., Simulations of non-linear fracture process zone in cementitious material a boundary element approach, *J. Comput. Mech.*, **7**, pp. 413-427, 1991

[35] Hartmann, F., Computing the c-matrix on non-smooth boundary points, in *New development in boundary element methods*, Southampton (UK), CNL Publications, pp. 367-379, 1980.

[36] Björck, Â. *Numerical Methods for Least Squares Problems*, SIAM, 1996

[37] Tikhonov, A.N., Arsenin, V.Y., *Solutions of ill-posed problems*, J. Wiley, 1977

[38] Press, W.H., Teukolsky, S.A., Vetterling, W.T., Flannery, B.P., *Numerical Recipes in Fortran*, Cambridge University Press, Cambridge (USA), 1992

[39] Ferreira, M.D.C., Venturini, W.S., Inverse analysis for two-dimensional structures using the boundary element mathod, *Adv. Eng. Software*(submitted), 2009

[40] Bolzon, G., Fedele, R., Maier, G., Parameter identification of a cohesive crack model by Kalman Filter, *Comp. Meth. Appl. Mech. Eng.*, **191**, pp. 2947-2871, 2002

[41] Hild, F., Roux, S., Digital image correlation: From measurement to identification of elastic properties - A review, *Strain*, **42**, pp. 69-80, 2006

[42] Besnard, G., Hild, F., Roux, S., ``Finite-element'' displacement fields analysis from digital images: Application to Portevin-Le Châtelier bands, *Exp. Mech.*, **46**, pp. 789-803, 2006

[43] Roux, S., Hild, F., Viot, P., Bernard, D., Three dimensional image correlation from X-Ray computed tomography of solid foam, *Comp. Part A*, **39**(8), pp. 1253-1265, 2008

[44] Limodin, N., Réthoré, J., Buffière, J.-Y., Gravouil, A., Hild, F., Roux, S., Crack closure and stress intensity factor measurements in nodular graphite cast iron using 3D correlation of laboratory X ray microtomography images, *Acta Mat.*, **57**(14), pp. 4090-4101, 2009

[45] Rannou, J., Limodin, N., Réthoré, J., Gravouil, A., Ludwig, W., Baïetto-Dubourg, M.-C., Buffière, J.-Y., Combescure, A., Hild, F., Roux, S., Three dimensional experimental and numerical multiscale analysis of a fatigue crack, *Comp. Meth. Appl. Mech. Eng.*, **199**, pp. 1307-1325, 2010

Figure captions

Figure 1: Sub-domain discretization and internal points.

Figure 2: Schematic view of the test and corresponding reference picture. Lengths are expressed in mm.

Figure 3: Standard displacement uncertainty vs. element size. The symbols are data obtained with the a priori analysis, and the dashed line is a power law fit using Equation (12).

Figure 4: Location of the two zones (dashed boxes) in the picture used to measure the displacement jump close to the notch.

Figure 5: -a-Load versus notch opening. The squares depict when the pictures were shot. -b-Notch opening versus crack opening displacement measured by DIC. The straight line is a linear interpolation.

Figure 6: Five horizontal displacement maps corresponding to crack propagation. The analyzed pictures are shown in the load versus notch opening plot. The physical size of one pixel is 54 µm. The picture number is defined in the load vs. notch opening plot.

Figure 7: -a-Horizontal displacement of a picture after sample failure. The physical size of one pixel is 54 µm.

-b-Crack surface determined from the 0-contour of the horizontal displacement (solid line). The dashed lines show the locations for which the displacement jumps are evaluated.

Figure 8: Crack surface superimposed on the deformed picture used to determine the displacement map of Figure 7a. A good match is observed.

Figure 9: Displacement jump along the crack surface as a function of picture number (Figure 6). This type of information will be used to identify the cohesive model.

Figure 10: Beam discretization and internal point used to evaluate Young's modulus.

Figure 11: Load displacement curve for the considered point (Figure 10) and the linear part used for the identification of Young's modulus.

Figure 12: Region of interest. Boundary and crack surface discretizations, and inner nodes.

Figure 13: Computed crack opening displacements for a given load level when the nodes are not allowed to interpenetrate.

Figure 14: Computed tractions along the crack surface.

Figure 15: Identified (solid symbols) and interpolated (solid line) crack opening displacements as a function of the corresponding tractions for the first cracked part (nodes 9 to 23). The confidence interval (dashed lines) is defined by $\pm 3\sigma_u$.

Figure 16: Identified (solid symbols) and interpolated (solid line) crack opening displacements as a function of the corresponding tractions for the second cracked part (nodes 25 to 35). The confidence interval (dashed lines) is defined by $\pm 3\sigma_u$.

Figure 17: Identified (solid symbols) and interpolated (solid line) crack opening displacements as a function of the corresponding tractions for both cracked parts. The confidence interval (dashed lines) is defined by $\pm 3\sigma_u$.

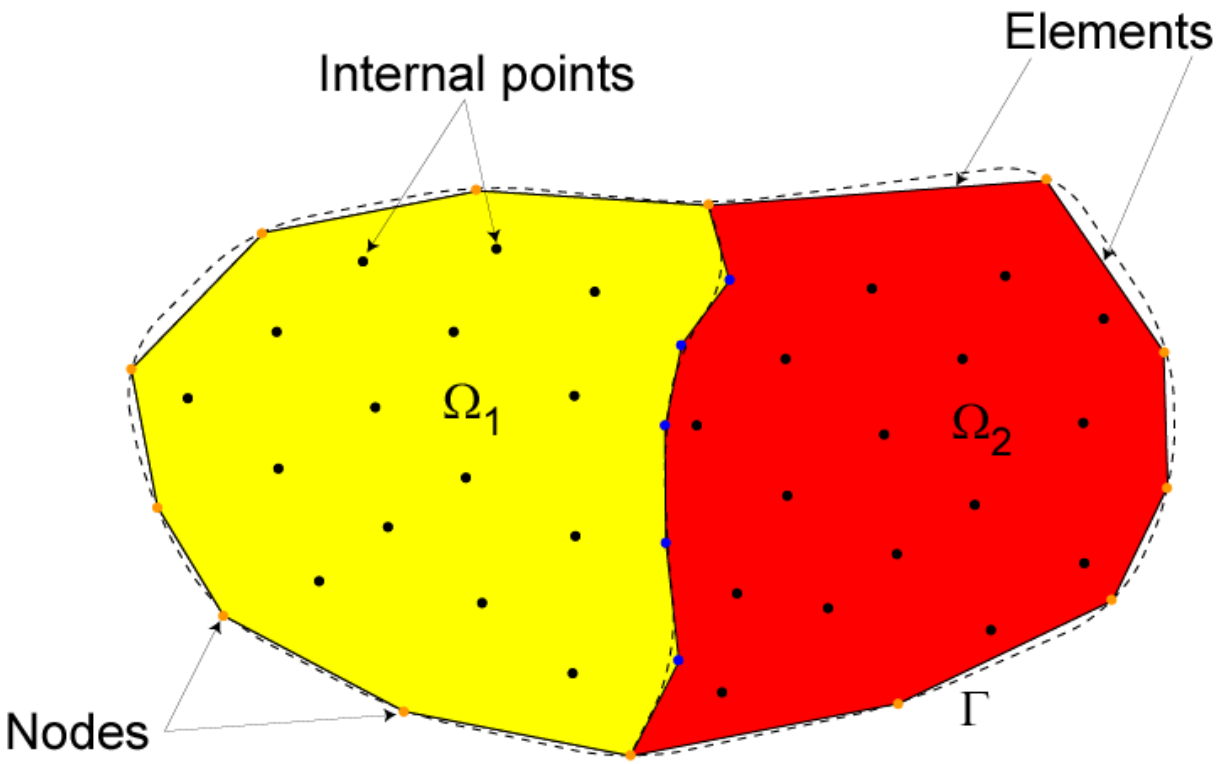

Figure 1.

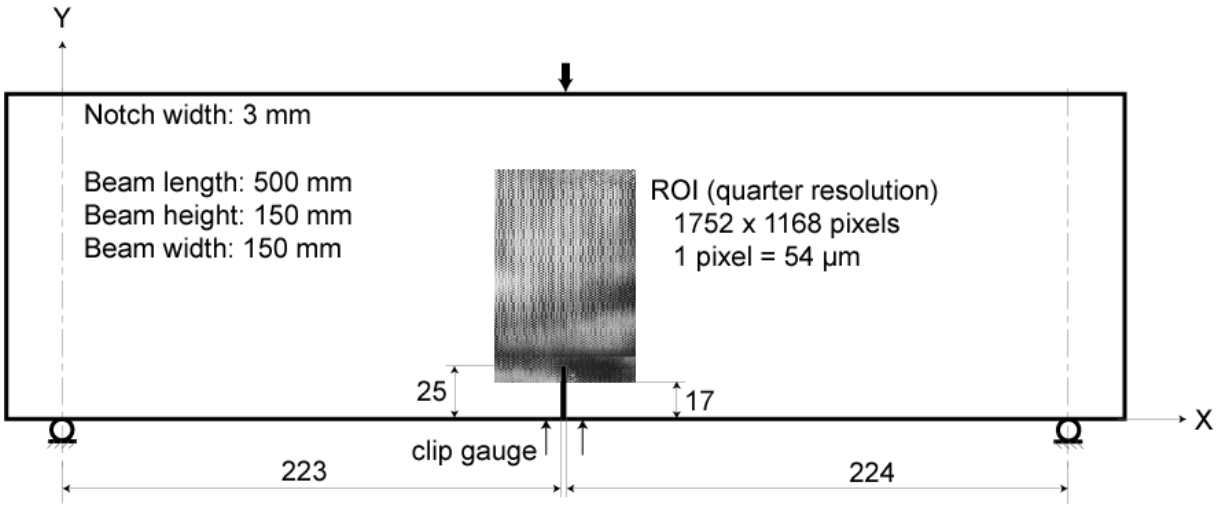
Y
Notch width: 3 mm
Beam length: 500 mm
Beam height: 150 mm
Beam width: 150 mm
ROI (quarter resolution)
1752 x 1168 pixels
1 pixel = 54 µm
25
17
X
clip gauge
223
224

Figure 2.

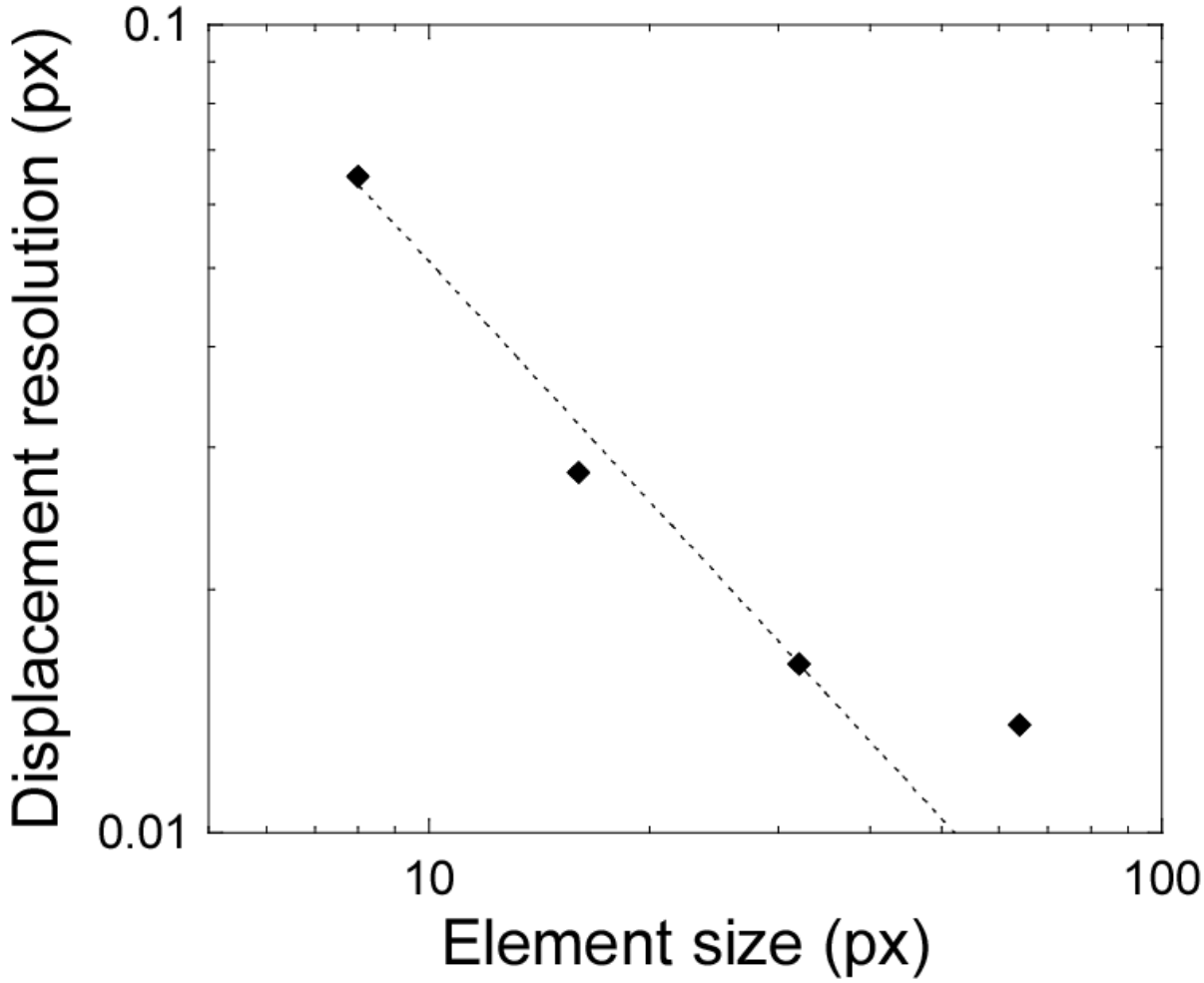

Figure 3.

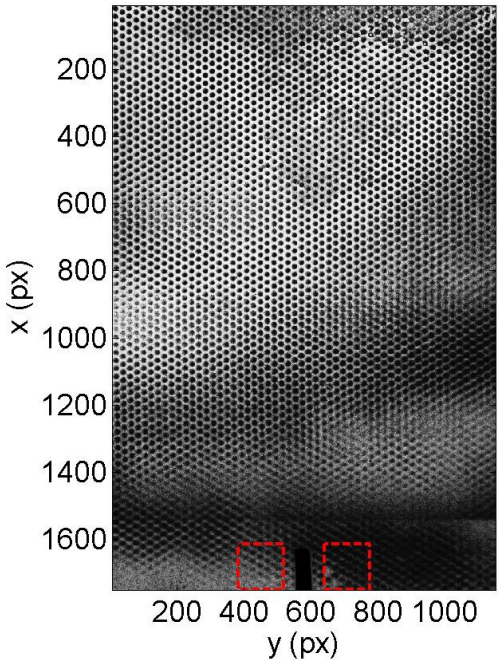
200
400
600
800
1000
1200
1400
1600
x (px)
200 400 600 800 1000
y (px)

Figure 4.

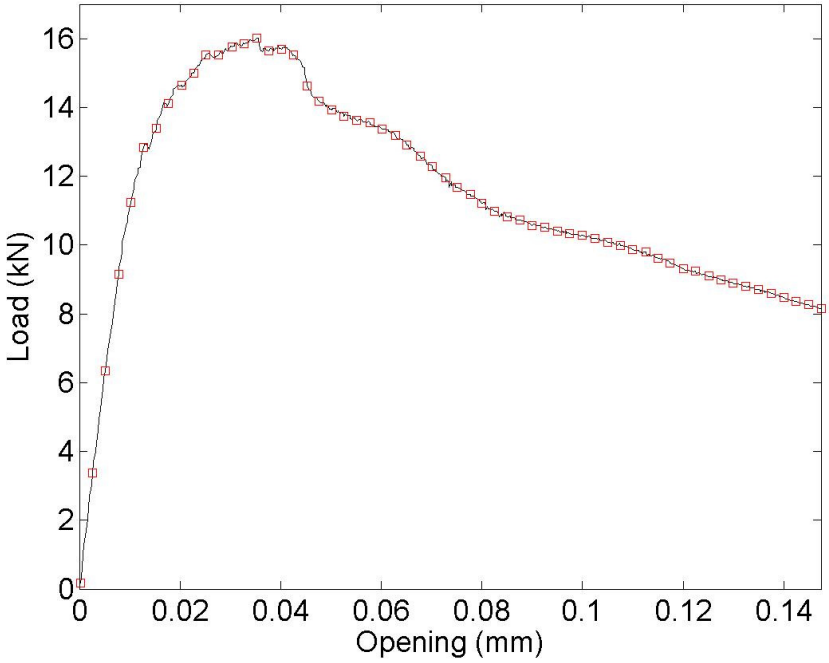
Load (kN)
Opening (mm)
0
2
4
6
8
10
12
14
16
0
0.02
0.04
0.06
0.08
0.1
0.12
0.14

-a-

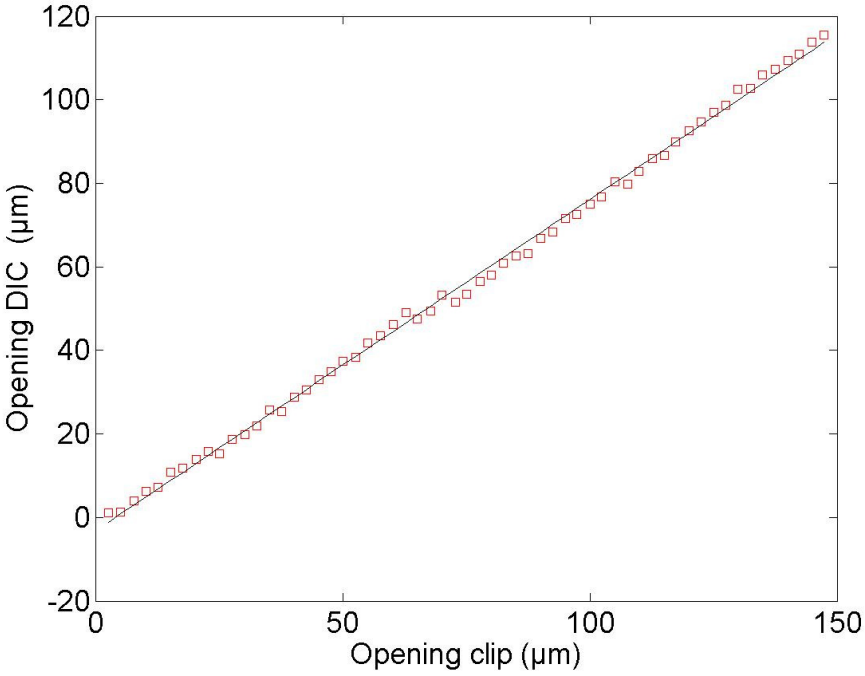
Opening DIC (µm)
Opening clip (µm)
-20
0
20
40
60
80
100
120
0
50
100
150

-b-

Figure 5.

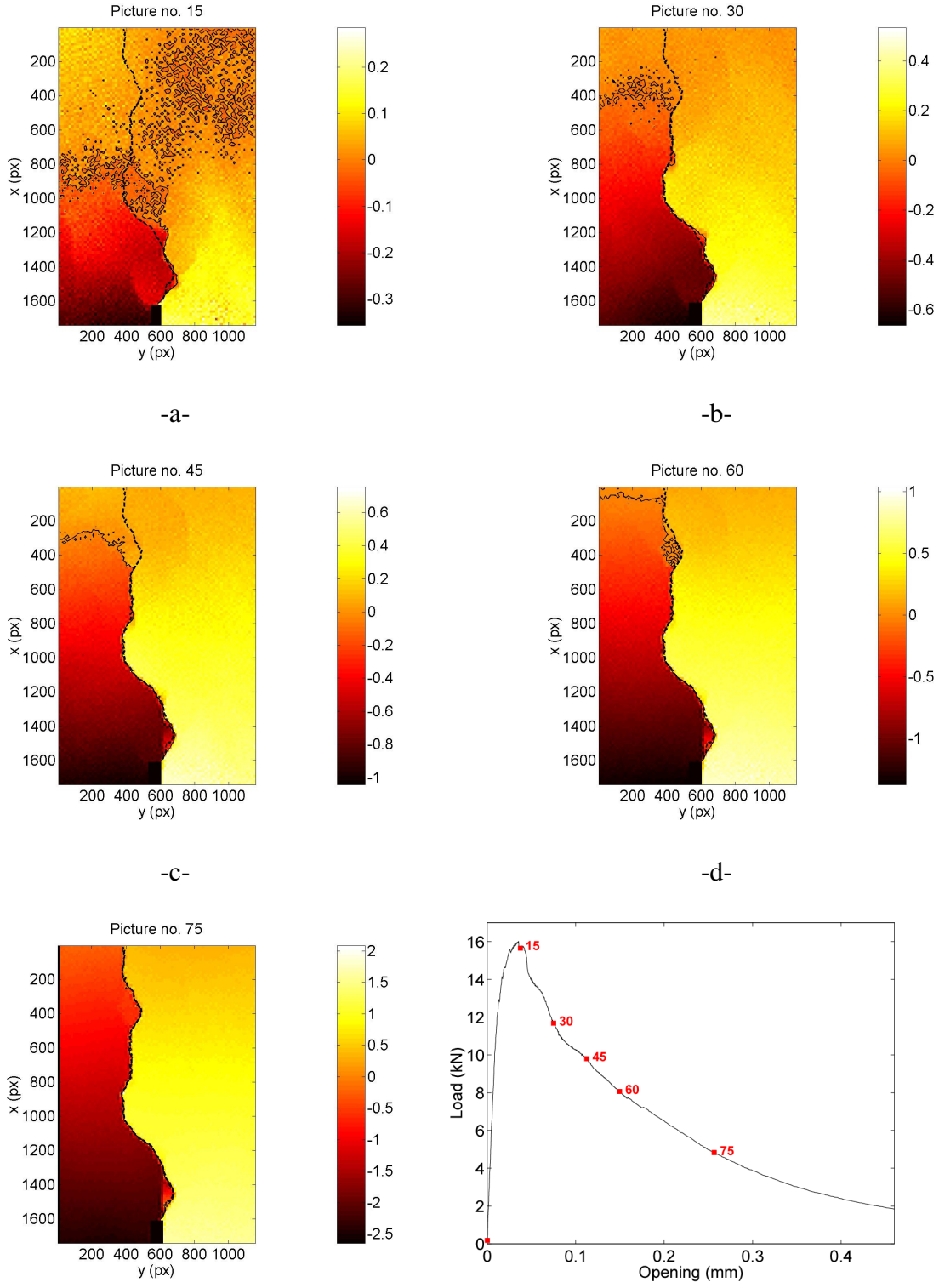

-a- -b-

-c- -d-

-e- -f-

Figure 6.

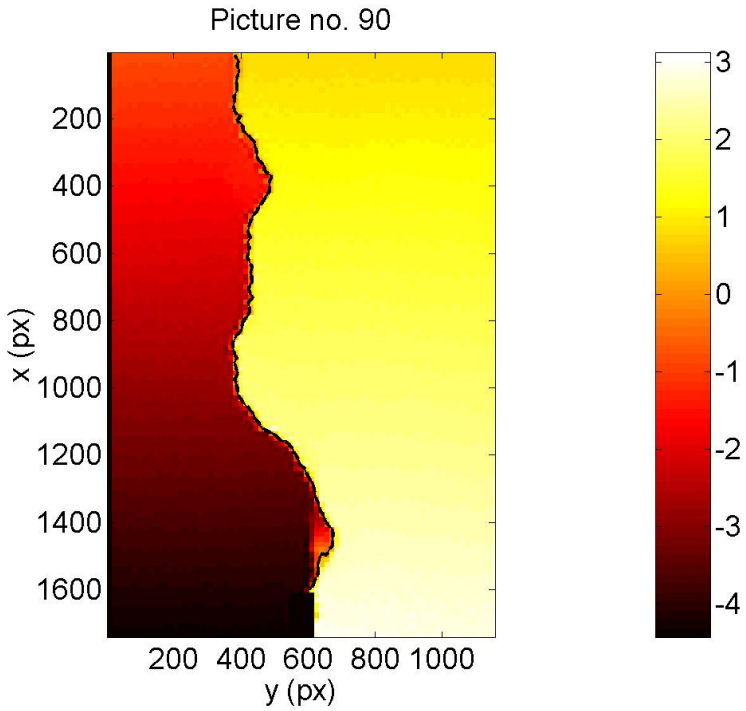
Picture no. 90
200
400
600
800
1000
1200
1400
1600
x (px)
200 400 600 800 1000
y (px)
3
2
1
0
-1
-2
-3
-4

-a-

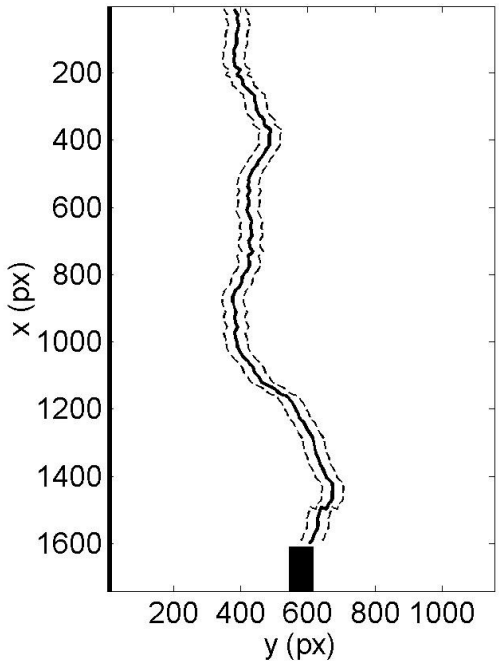
200
400
600
800
1000
1200
1400
1600
x (px)
200 400 600 800 1000
y (px)

-b-

Figure 7.

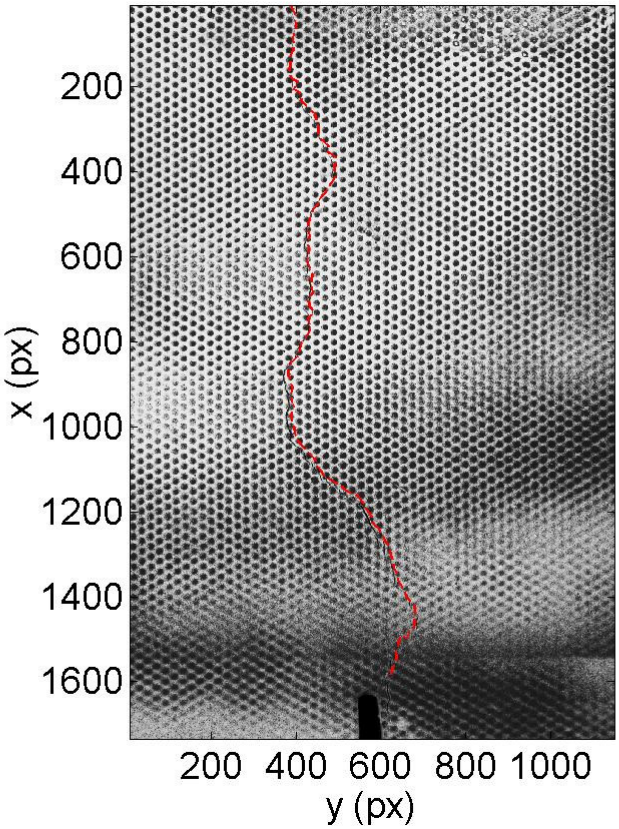
200
400
600
800
1000
1200
1400
1600
x (px)
200 400 600 800 1000
y (px)

Figure 8.

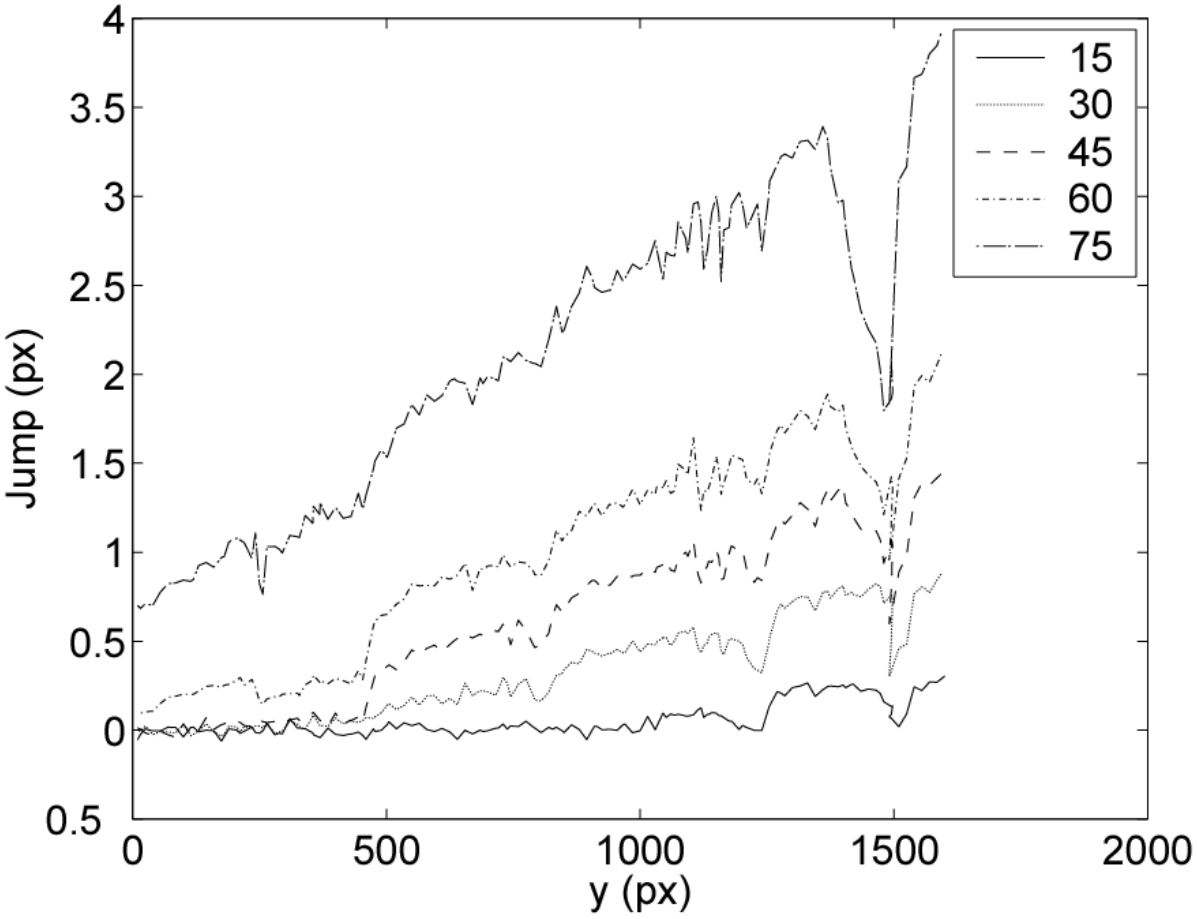
15
30
45
60
75
Jump (px)
y (px)
4
3.5
3
2.5
2
1.5
1
0.5
0
0.5
0
500
1000
1500
2000

Figure 9.

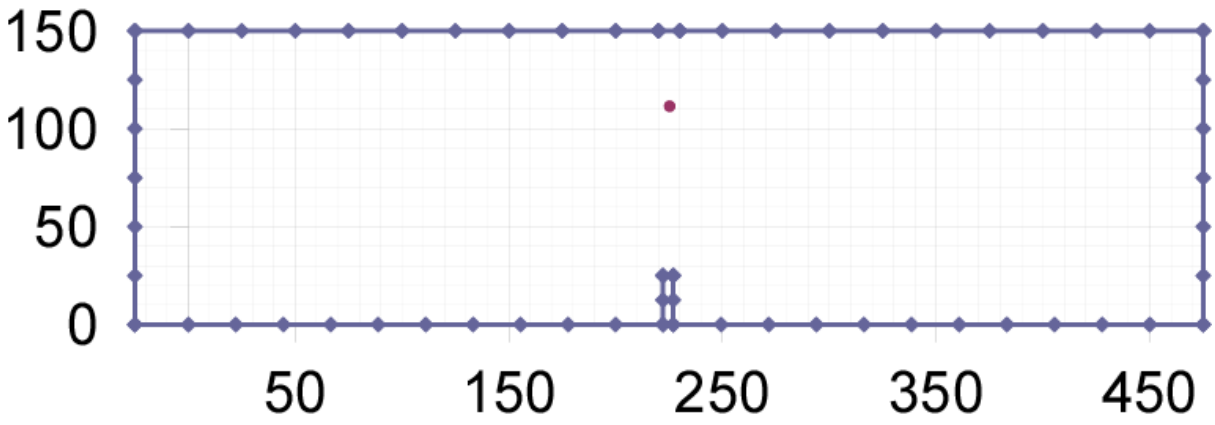

Figure 10.

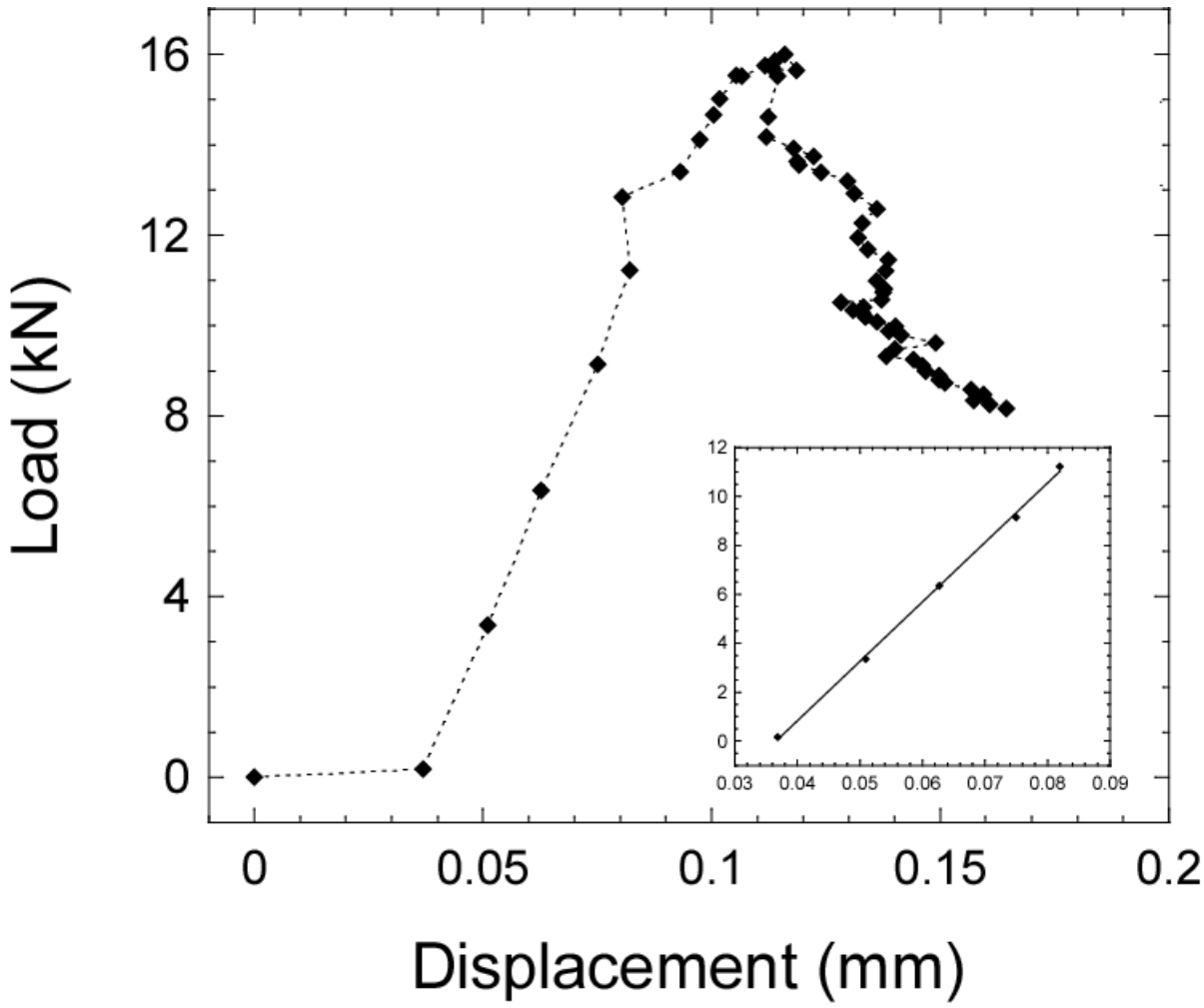
Load (kN)
Displacement (mm)
0
4
8
12
16
0
0.05
0.1
0.15
0.2
0
2
4
6
8
10
12
0.03
0.04
0.05
0.06
0.07
0.08
0.09

Figure 11.

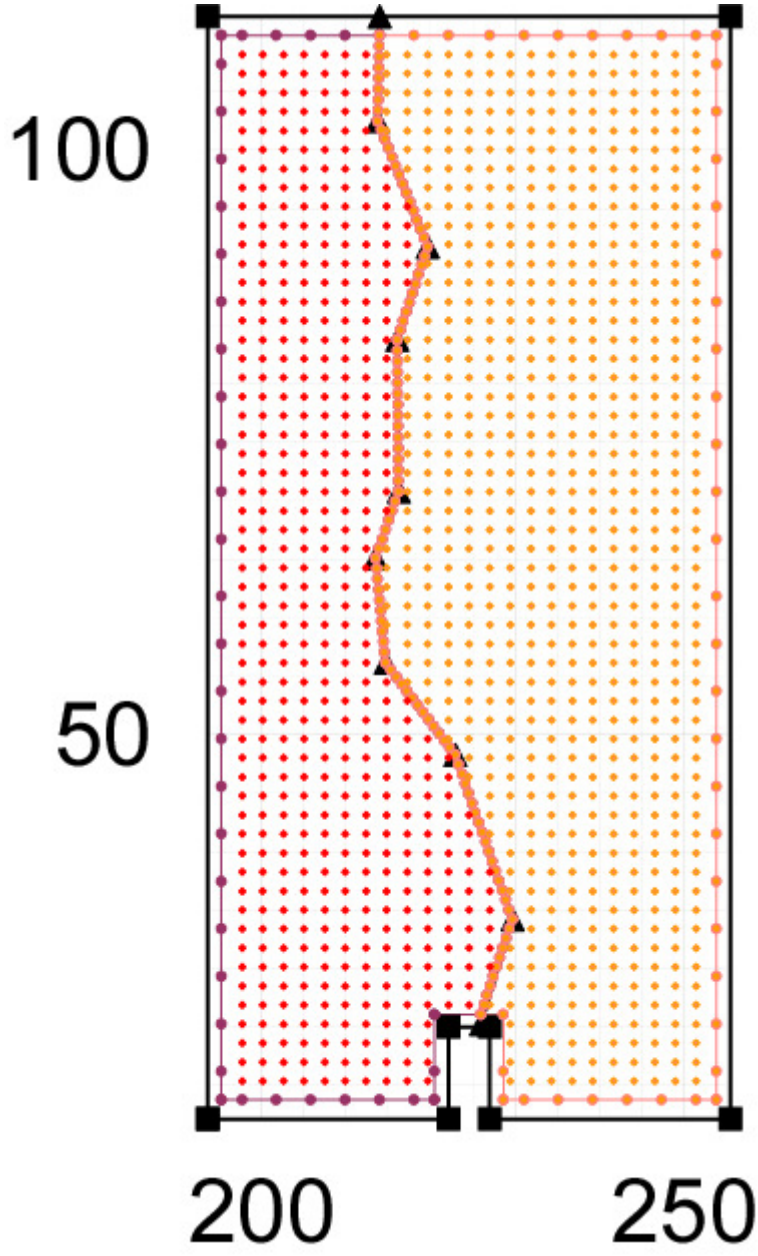

Figure 12.

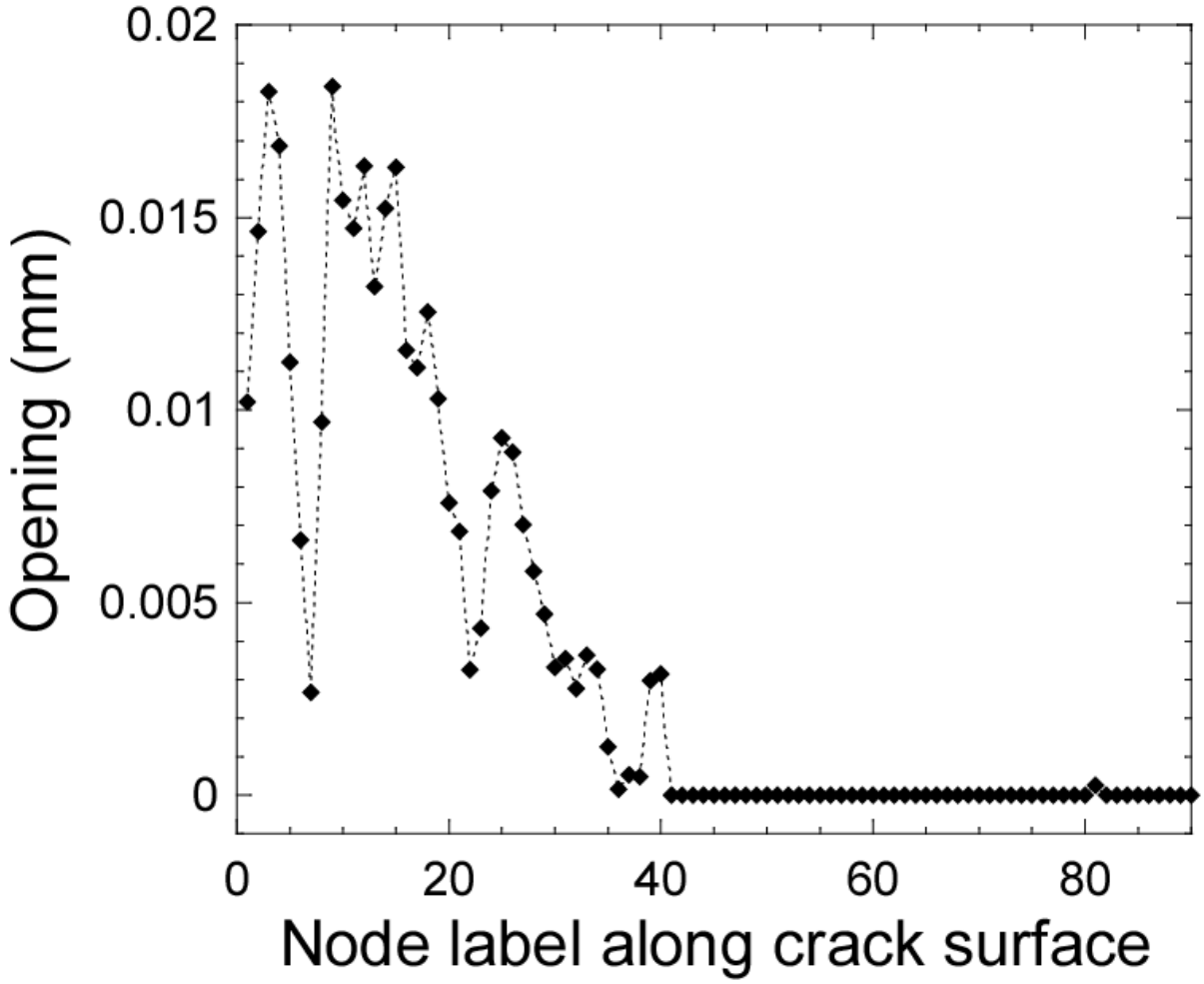
0.02
0.015
0.01
0.005
0
Opening (mm)
0
20
40
60
80
Node label along crack surface

Figure 13.

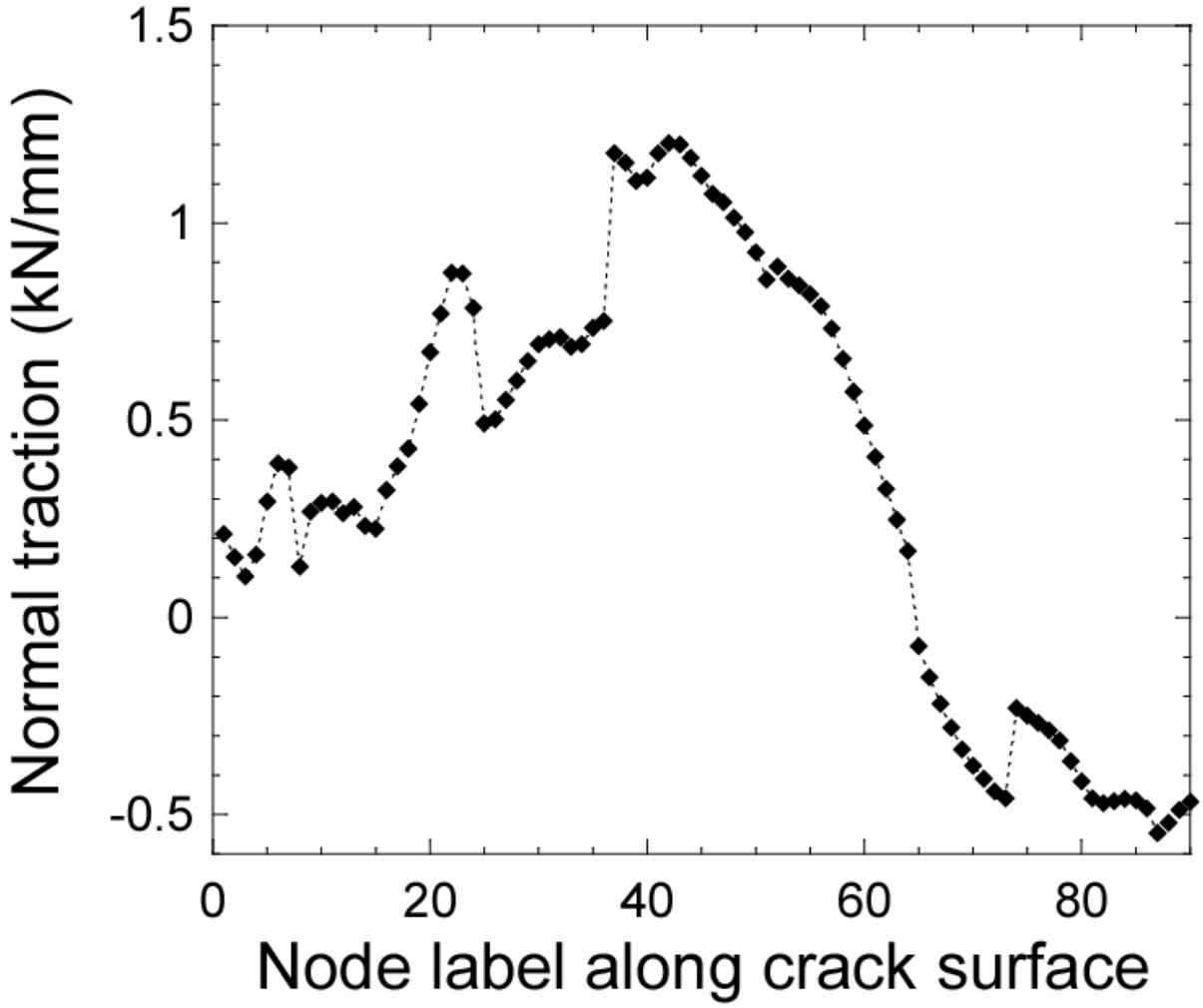
Normal traction (kN/mm)
1.5
1
0.5
0
-0.5
0
20
40
60
80
Node label along crack surface

Figure 14.

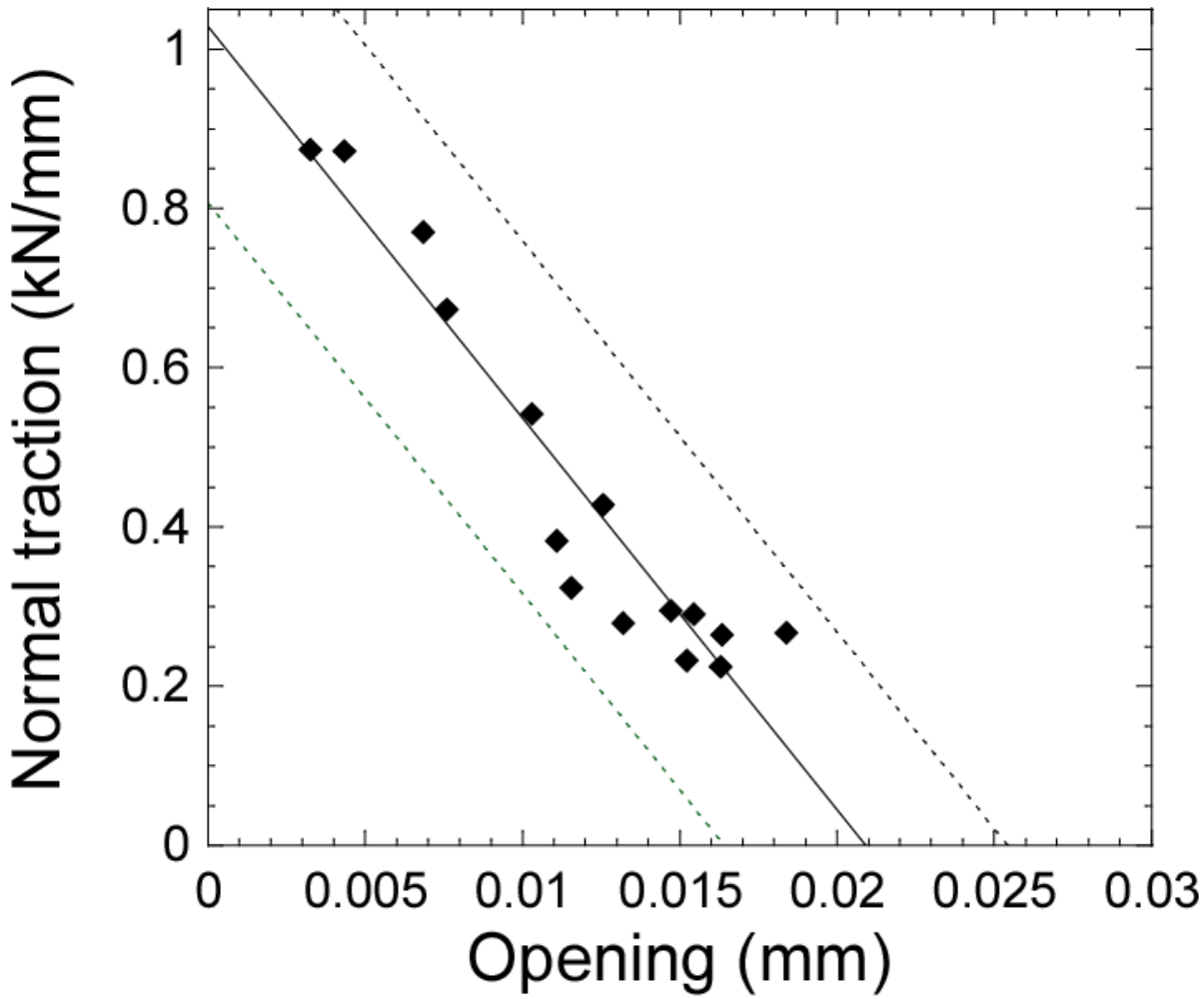
Normal traction (kN/mm)
1
0.8
0.6
0.4
0.2
0
0
0.005
0.01
0.015
0.02
0.025
0.03
Opening (mm)

Figure 15.

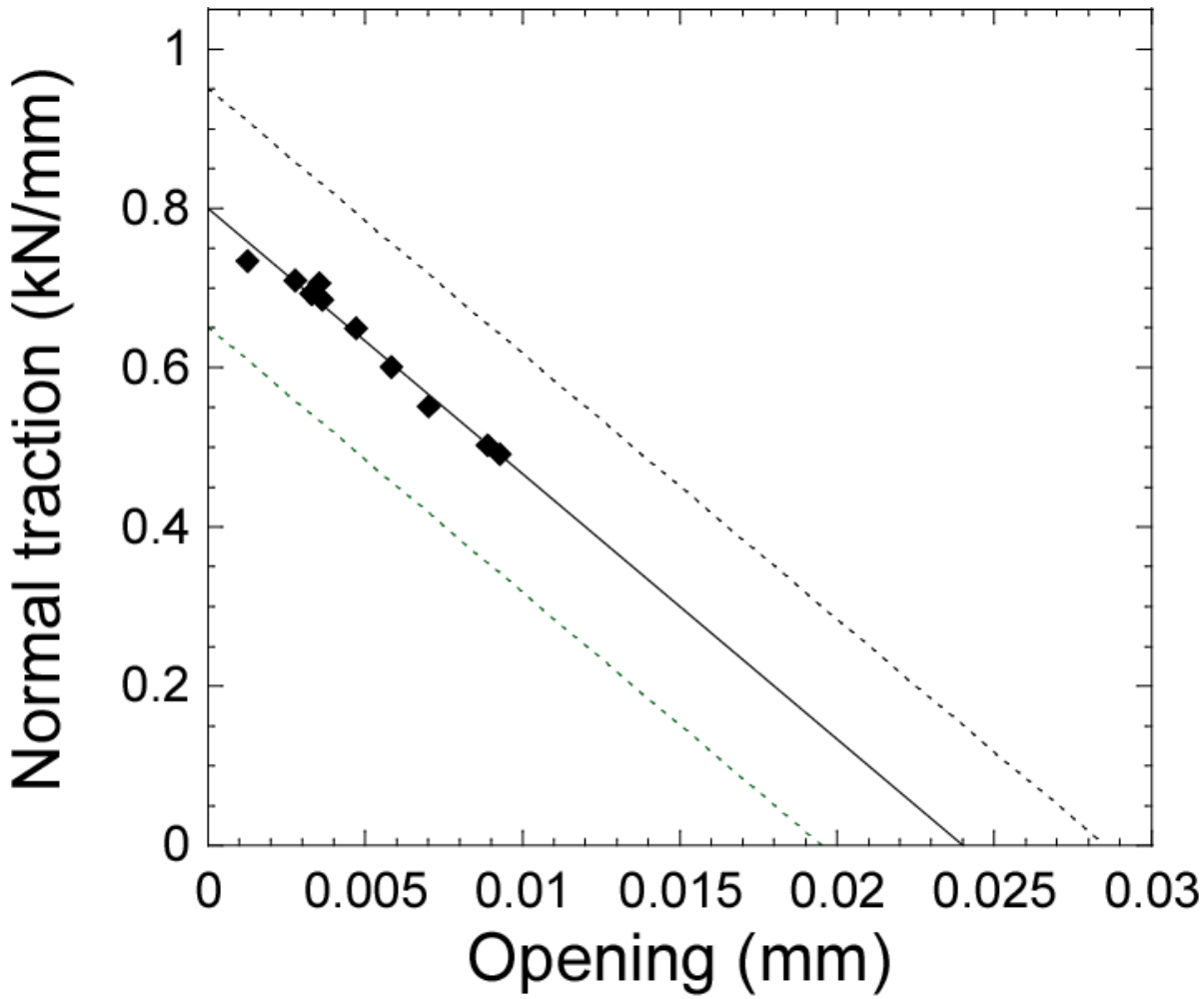
Normal traction (kN/mm)
1
0.8
0.6
0.4
0.2
0
0
0.005
0.01
0.015
0.02
0.025
0.03
Opening (mm)

Figure 16.

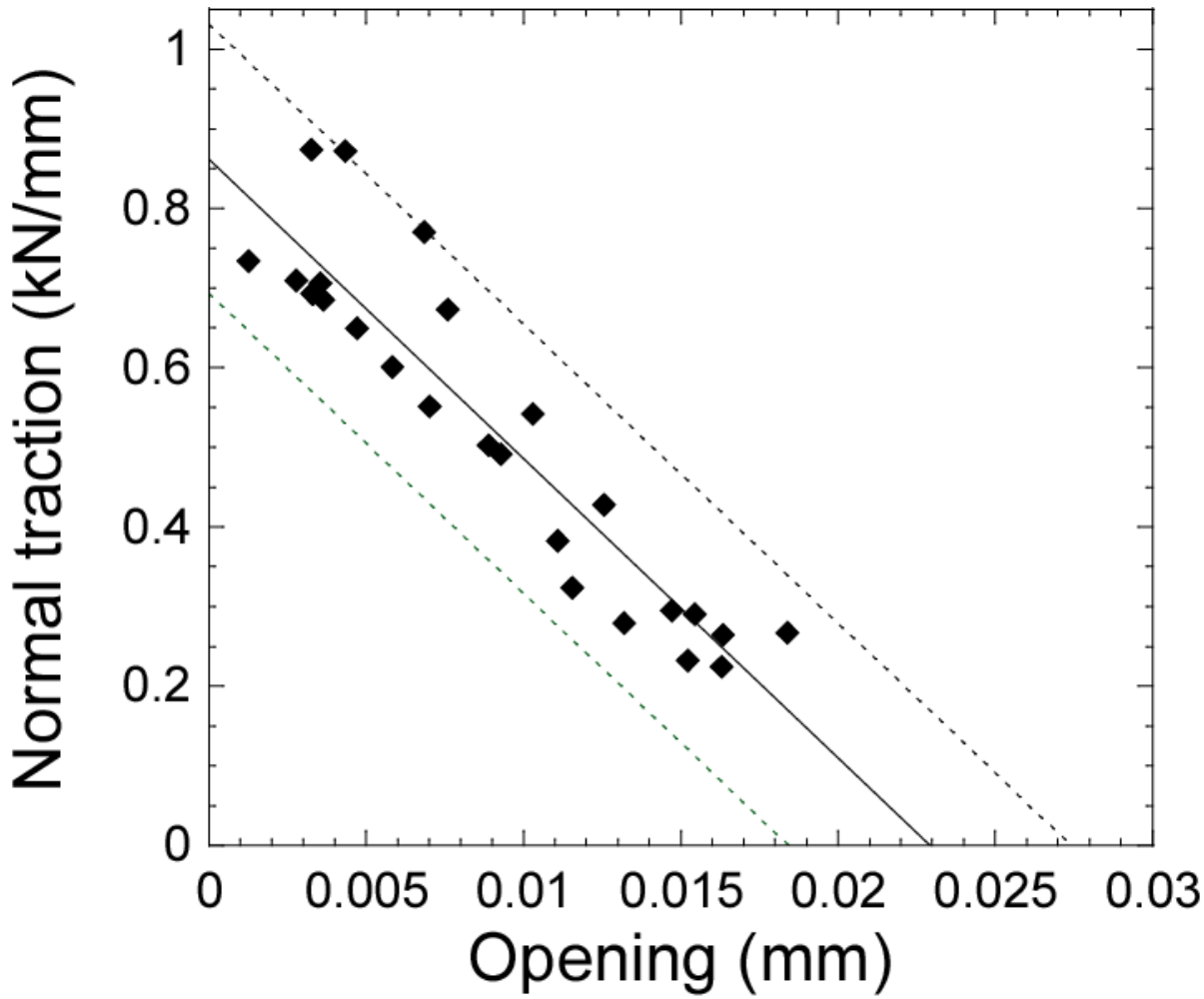
Normal traction (kN/mm)
1
0.8
0.6
0.4
0.2
0
0
0.005
0.01
0.015
0.02
0.025
0.03
Opening (mm)

Figure 17.